Polydisperse particles in an irradiated turbulent gas-particle mixture

By M. Rahmani, G. Geraci, G. Iaccarino AND A. Mani

1. Motivation and objectives

The present study has been motivated by solid particle solar receivers (SPR) that use solid particles, laden in a carrier gas, to directly absorb concentrated solar radiation (Siegel *et al.* 2010). To investigate the performance of SPRs, it is necessary to understand the complex three-way coupling between the gas flow, particle transport and radiative heat transfer. This three-way coupling gives rise to many multi-physics phenomena that, other than SPRs, also have application in many industrial and natural flows such as cloud physics, volcanic eruptions, solid rocket motors, and droplet combustion. A three-way coupled system of homogeneous and isotropic turbulence, laden with particles with buoyancy effects, and in an irradiated environment was studied by Zamansky *et al.* (2014), using direct numerical simulations (DNS), point particle models, and a constant radiation intensity in an optically thin environment. This study revealed how non-uniformities in concentration of particles contribute to local heating of the fluid, and therefore buoyancy-induced vortices that sustain turbulence. For a convective flow of gas and particles subject to radiation and without buoyancy effects, using the same numerical methods of Zamansky *et al.* (2014), Pouransari & Mani (2015) showed that different particle concentration patterns at different Stokes numbers significantly influence the heat transfer from particles to gas. While both these studies considered single-size particles, the solid particles used in SPRs are polydisperse, i.e., their size varies over a relatively wide range. Our interest here is to investigate the effects of polydispersity on particle preferential concentration and thermal performance of SPRs for the same physical problem of Pouransari & Mani (2015).

Key questions are how different classes of particles in polydisperse particles contribute to the overall particle clustering, and whether a certain particle size class can represent the physics of the entire particle size distribution. In turbulent particle-laden flows, preferential concentration refers to the accumulation of particles in regions of high strain rates, where particles are centrifuged out of regions of high vorticity due to particle and flow vortices interactions (Maxey 1987; Squires & Eaton 1991; Eaton & Fessler 1994). It is well known from the literature that the strongest preferential concentration occurs at particle Stokes numbers close to 1.0 (Balachandar & Eaton 2010). Previous studies also suggest that particle clustering can significantly modify flow and turbulence properties (Elghobashi & Truesdell 1993; Sundaram & Collins 1999). However, for polydisperse particles, where different-size particles can simultaneously acquire a wide range of particle Stokes number, characterizing the particle-clustering regimes may not be solely dependent on a sample averaged or particle class representative Stokes number due to the interactions of different classes of particle sizes. Moreover, the problem of SPRs involves several physical parameters, where finding a particle size that represents a monodisperse equivalent particle size by matching all these parameters between monodisperse and polydisperse particles might not be feasible.

This report is organized as follows. Section 2 describes the physics of the problem, important dimensionless parameters, and our choices of these parameters for this study, as well as a brief overview of the numerical methods to solve the governing equations. In Section 3, we present a one-dimensional model for the problem, and compare its predictions to the results of DNS. Next, we analyze the energy balance of the system in Section 4. The particle-clustering patterns for monodisperse and polydiperse cases are examined in Section 5. The conclusions are stated in Section 6.

2. Physical problem and numerical approach

2.1. *Problem description*

A square channel $L \times W \times W$ in size, with x, y and z denoting the streamwise, spanwise, and vertical directions, respectively, is considered. A turbulent mixture of gas and particles enters the channel at the mean velocity U_0 and with the initial temperature T_0. We neglect the gravitational force in this study as its effect is negligible compared to the inertia of the inflow. The boundary conditions of the domain in y and z directions are periodic. As the gas and particles flow through the channel they are irradiated at a constant radiation intensity I_0. We assume an optically thin mixture, which implies that all particles receive the same radiation intensity. Due to the heating of the particles, and heat transfer from the particles to the gas, the flow accelerates along x direction. The carrier gas is air, with constant viscosity μ, isochoric specific heat capacity, C_p, isobaric specific heat capacity, C_v, and thermal conductivity k. The average gas temperature, T_g, rises through x direction as the gas gets heated by the particles, and hence its density ρ drops, with ρ_0 denoting the gas density at the inlet. We consider spherical particles with variable (polydisperse) or constant (monodisperse) diameter, D_p, and constant density ρ_p, constant specific heat capacity, C_{vp}, and constant thermal conductivity k_p. The emissivity of these particles in an optically thin medium is denoted by ϵ_p. The particle loading of the system is measured by the particle number density, n_p, which is n_0 at the inlet and decreases along the channel as the flow accelerates and the mixture is diluted.

We describe the variable particle diameter with the probability density function f_{D_p}, defined over the compact $[D_p^{\min}, D_p^{\max}]$. The method of construction of this PDF is given in detail by Rahmani *et al.* (2015). We assume N_S number of particle classes with equal Euclidean measure $\Delta D_p = (D_p^{\max} - D_p^{\min})/N_S$. Any kth class is represented by the diameter D_{p_k}, and relative frequency $\omega_k\,(D_{p_k}) = \dfrac{n_{p_k}}{n_0}$, with $\sum_{k=1}^{N_S} \omega_k = 1$ holding.

By employing the PDF description for polydisperse particles, and choosing a nominal mass loading ratio, we find a diameter and particle number density for monodisperse particles so that the two systems are thermodynamically equivalent, which requires matching of the total mass loading ratio of particles, M.L., and the total frontal area ratio of particles, F.A., between monodisperse and polydisperse particles. These two nondimensional parameters are defined as

$$\text{M.L.} = \frac{\pi \rho_p n_0}{6 \rho_g} \sum_{k=1}^{N_S} \omega_k D_{p_k}^3, \quad \text{and} \quad \text{F.A.} = \frac{W \pi n_0}{4} \sum_{k=1}^{N_S} \omega_k D_{p_k}^2, \tag{2.1}$$

where for monodisperse particles $N_S = 1$ should be applied. The details of the design of monodisperse particles is described by Rahmani *et al.* (2015). We chose a nominal mass loading ratio of $\widehat{\text{M.L.}} = 0.13$, which gave $\widehat{\text{F.A.}} = 0.11$, $n_0^{\text{mono}} = 3.3 \times 10^{10}$ m^{-3} for monodisperse particles, and $n_0^{\text{poly}} = 4.15 \times 10^{10}$ m^{-3} for polydisperse parti-

cles, and $D_p^{\mathrm{mono}} = 1.016 \times 10^{-5}$ m for monodisperse particles. Hence, using this design the number of polydisperse particles is higher than that of the monodisperse particles: $n_0^{\mathrm{poly}} = 1.26 n_0^{\mathrm{mono}}$. This difference implies that the second and third moments of the PDF of the particle size for polydisperse particles are 26% lower than D_p^2 and D_p^3 for monodisperse particles.

2.2. *Dimensionless parameters and choices of simulations*

The particle Stokes number is defined as

$$St_\eta = \frac{\tau_p}{\tau_\eta}. \tag{2.2}$$

In this definition, τ_p is the particle relaxation time, defined as

$$\tau_p = \frac{\rho_p D_p^2}{18\mu}, \quad \text{and} \quad \tau_\eta = \left(\frac{\mu}{\rho\varepsilon}\right)^{1/2}, \tag{2.3}$$

is the Kolmogorov time scale of the flow, with ε being the volume averaged rate of dissipation of turbulent kinetic energy. In our simulations, the forced turbulence in the box domain is set to have a rate of dissipation of kinetic of energy of $\varepsilon = U_0^3/(100W)$, an approximation for the wall-induced turbulence in the main channel. Based on this approximation, the Kolmogorov time scale is $\tau_\eta = (10W/U_0)Re_W^{-1/2}$, where

$$Re_W = \frac{\rho U_0 W}{\mu} \tag{2.4}$$

is the large-scale Reynolds number of the flow. We also introduce a sample averaged relaxation time scale for polydisperse particles

$$\tau_p^{\mathrm{SA}} = \sum_{k=1}^{N_S} \omega_k \tau_{pk} = \frac{\rho_p}{18\mu} \sum_{k=1}^{N_S} \omega_k D_{p_k}^2, \tag{2.5}$$

which provides a bulk measure of the average relaxation time for particle size distribution. Based on this particle relaxation time, a sample averaged Stokes number can be defined as

$$St_\eta^{\mathrm{SA}} = \frac{\tau_p^{\mathrm{SA}}}{\tau_\eta}. \tag{2.6}$$

Here we vary the Stokes number by varying τ_η via changing the inlet velocity U_0. Therefore, as presented in Table 1, we consider four different cases for which the inlet Stokes number, St_{η_0}, and the Reynolds number, Re_W, vary simultaneously. The objective is to compare monodisperse and polydisperse particles for each case. Our monodisperse particle Stokes numbers span a range from $St_{\eta_0} = 0.1$ to 4.0. This range includes $St_{\eta_0} = 1.0$, the Stokes number of maximum preferential concentration of particles, as reported in the literature (Squires & Eaton 1991; Eaton & Fessler 1994; Pouransari & Mani 2015). The range of sample averaged Stokes numbers for polydisperse particles is lower: $0.08 \leqslant St_{\eta_0}^{\mathrm{SA}} \leqslant 3.2$.

Another interesting measure of the turbulent flow is the Taylor Reynolds number, Re_λ, which measures the strength of the inertia of intermediate size eddies, and is defined based on the Taylor length scale, λ, and u_{rms}:

$$Re_\lambda = \frac{\rho u_{rms} \lambda}{\mu} \sim Re_W^{1/2}, \quad \text{where} \quad \lambda = \left(\frac{15\mu u_{rms}^2}{\rho\varepsilon}\right)^{1/2}. \tag{2.7}$$

No	Re_W	Re_λ	$St_{\eta_0}^{\text{mono}}$ $St_{\eta_0}^{\text{SA}}$ (poly, range)	$\mathcal{R}^{\text{mono}}$ $\mathcal{R}^{\text{SA}}$ (poly, range)	$\mathcal{R}^{'\text{mono}}$ $\mathcal{R}^{'\text{SA}}$ (poly, range)	η/L $\times 10^{-3}$
case1:	1,124	20	0.1 0.08 (0.02 - 0.21)	0.09 0.08 (0.04 - 0.13)	26.5 33.8 (18.1 - 58.2)	4.0
case 2:	2,830	32	0.4 0.32 (0.08 - 0.85)	0.23 0.20 (0.1 - 0.33)	26.3 33.6 (18.1 - 57.8)	2.0
case 3:	5,217	43	1.0 0.8 (0.21 - 2.13)	0.42 0.36 (0.19 - 0.62)	26.1 33.5 (17.9 - 57.4)	1.3
case4	13,135	68	4.0 3.2 (0.83 - 8.5)	1.05 0.89 (0.48 - 1.52)	25.7 32.8 (17.6 - 56.5)	0.64

Table 1: Dimensionless parameters for different cases studied. In all cases the particle mass loading ratio, M.L. = 0.13, and the particle frontal area ratio, F.A. = 0.11. The number of grid points in the spanwise and vertical directions are: $N_y = N_z = N_x/4$, where $N_x = 512$, 512, 512, and 1024, for cases 1, 2, 3, and 4, respectively.

To resolve the smallest scales of the flow, an isotropic mesh with size $N_x \times N_y \times N_z$ has been chosen so that $L/N_x = W/N_y = W/N_z \leq \pi\sqrt{2}/3\eta$, a DNS resolution requirement suggested by Eswaran & Pope (1988), where $\eta = \left(\mu^3/(\rho^3\varepsilon)\right)^{1/4}$ is the Kolmogorov length scale of the flow.

The radiation intensity for each case has been chosen so that the increase in the mean gas temperature at the outlet is the same for all cases. The dimensionless radiation intensity (and its sample averaged quantity) can be defined in two ways:

$$\mathcal{R} = \frac{\epsilon_p I_0 D_p}{8kT_0}, \quad \text{and} \quad \mathcal{R}^{\text{SA}} = \frac{\epsilon_p I_0}{8kT_0}\sum_{k=1}^{N_S}\omega_k D_{p_k}, \quad \text{or} \tag{2.8}$$

$$\mathcal{R}^{'} = \frac{3\epsilon_p I_0 L}{2\rho_p C_{vp} T_0 U_0 D_p} \quad \text{and} \quad \mathcal{R}^{'\text{SA}} = \frac{3\epsilon_p I_0 L}{2\rho_p C_{vp} T_0 U_0}\sum_{k=1}^{N_S}\frac{\omega_k}{D_{p_k}}. \tag{2.9}$$

The first definition, $\mathcal{R}$, measures the rate of radiation absorption by a particle relative to the rate of conductive heat transfer from the particle, while the second definition, $\mathcal{R}^{'}$, measures the rate of radiation absorption by a particle compared to the convective rate of transfer of the thermal energy of the particle. The sample averaged parameters, similarly, extend these definitions to an average over all particles. Table 1 shows that $\mathcal{R}$

increases with increasing St_η for different cases and is higher for monodisperse particles. But $\mathcal{R}^{'}$ has a small Reynolds number dependence (as the outlet gas temperature is fixed) and acquires higher sample averaged values for polydisperse particles.

2.3. *Governing equations*

The motion of the gas phase is described by conservation of mass

$$\frac{\partial \rho}{\partial t} + \frac{\partial}{\partial x_j}\left(\rho u_j\right) = 0, \tag{2.10}$$

and conservation of momentum

$$\frac{\partial}{\partial t}\left(\rho u_i\right) + \frac{\partial}{\partial x_j}\left(\rho u_i u_j\right) = -\frac{\partial p}{\partial x_i} + \mu \frac{\partial}{\partial x_j}\left(\frac{\partial u_i}{\partial x_j} + \frac{\partial u_j}{\partial x_i} - \frac{2}{3}\frac{\partial u_k}{\partial x_k}\delta_{ij}\right) + f_i, \tag{2.11}$$

where $\vec{\boldsymbol{u}} = (u, v, w)$ is the gas velocity field, p is the gas hydrodynamic pressure field, and there is no gravitational force. In Eq. 2.11 $f_i(\vec{\boldsymbol{x}}, t)$ is the two-way momentum coupling force between the particle and gas phase for the unit volume, and stated as

$$f_i(\vec{\boldsymbol{x}}, t) = \sum_{k=1}^{N_S} \frac{m_{p_k}}{\tau_{p_k}} \sum_{j=1}^{N_k} \hat{\boldsymbol{e}}_i \cdot \left(\vec{\boldsymbol{u}}(\vec{\boldsymbol{x}}) - \vec{\boldsymbol{u}}_{p,j}\right) \delta(\vec{\boldsymbol{x}} - \vec{\boldsymbol{x}}_{p,j}), \tag{2.12}$$

where $m_{pk} = \pi \rho_p D_{pk}^3/6$ is the particle mass, $\vec{\boldsymbol{u}}_p = (u_p, v_p, w_p)$ is the particle velocity, and $\vec{\boldsymbol{x}}$ and $\vec{\boldsymbol{x}}_p$ denote the position vector for gas and particle, respectively. In equations above we have assumed a variable density low Mach number flow, for which $P = P_{th} + p$ and $p \ll P_{th}$, where P_{th} is the thermodynamic pressure and is constant due to the low Mach number assumption. The polytropic ideal gas law: $P_{th} = \rho R T_g$, with R being the ideal gas constant for air, hold in the channel. The energy equation for the gas phase then is written as

$$\frac{\partial}{\partial t}\left(\rho C_v T_g\right) + \frac{\partial}{\partial x_j}\left(\rho C_p T_g u_j\right) = k \frac{\partial^2 T_g}{\partial x_j \partial x_j} + \mathcal{S}, \tag{2.13}$$

where $\mathcal{S}$ is a source term for the gas energy equation, representing the heat transfer from the particle phase

$$\mathcal{S} = \pi \sum_{k=1}^{N_S} D_{p_k}^2 h_{p_k} \sum_{j=1}^{N_{p_k}} (T_{p,j} - T_g(\vec{\boldsymbol{x}}))\delta(\vec{\boldsymbol{x}} - \vec{\boldsymbol{x}}_{p,j}), \tag{2.14}$$

with $h_{pk} = Nuk/D_{pk}$ being the convection coefficient from particles to the gas. For small particle Reynolds numbers in this study $Nu \sim 2$. For our particles, the Biot number, $Bi = h_{pk} D_{pk}/k_p$, is very small so that the the particles are assumed to be isothermal.

The motion of particles is simulated using Lagrangian inertial point particles, a method that well suits our particles with range of diameters at least two orders of magnitude smaller than the Kolmogorov length scale of the flow. The position of each particle is tracked by

$$\frac{d\vec{\boldsymbol{x}}_p}{dt} = \vec{\boldsymbol{u}}_p, \tag{2.15}$$

while the velocity of the particle is found from the force balance on the particle

$$\frac{d\vec{\boldsymbol{u}}_p}{dt} = \frac{\vec{\boldsymbol{u}}(\vec{\boldsymbol{x}}) - \vec{\boldsymbol{u}}_p}{\tau_p}. \tag{2.16}$$

The right-hand side of the equation above is the Stokes drag calculated based on the slip velocity, the velocity difference between the particle, and the fluid at the location of the particle.

The thermal energy for a single Lagrangian particle is written as

$$\frac{d}{dt}\left(m_p C_{vp} T_p\right) = \frac{\pi D_p^2}{4}\epsilon I_0 + \pi D_p^2 h_p \left(T_g\left(\vec{\boldsymbol{x}}_{\boldsymbol{p}}\right) - T_p\right), \tag{2.17}$$

stating that the rate of increase of the thermal energy of a particle is equal to the rate at which it absorbs radiation over its frontal area minus the rate of heat transfer to its surrounding fluid.

2.4. *Numerical approach*

Equations (2.10)-(2.17), that describe the entire physics of the problem, are solved in three dimensions using direct numerical simulation (DNS) of tubulence for the gas phase, combined with Lagrangian point particle tracking, as described in detail by Pouransari & Mani (2015). The DNS code makes use of a second order central finite difference scheme on a staggered mesh for spatial discretization and interpolation, and a fourth-order Runge-Kutta scheme for advancing in time. A homogeneous, isotropic turbulent flow (without radiation), initially randomly laden with particles with particle number density of n_0, is generated in a three-dimensional triply periodic computational domain with dimensions $W \times W \times W$. In this domain the homogeneous isotropic turbulence (HIT) is sustained using a linear forcing (Rosales & Meneveau 2005) so that the turbulence intensity $\langle u_{rms} \rangle / U_0 \sim 0.12$ ($\langle\rangle$ denoting a volume and time averaging) for all simulations. The statistically steady results of the HIT and its seeded particles are used as an inflow for the main inflow/outflow computational domain at each timestep. The spatial and temporal numerical schemes, grid resolution, timestep, and momentum two-way coupling, are matched between the HIT and main computational domain.

3. One-dimensional model

A 1D approximation can be formulated for the flow of the mixture of particles and gas by assuming a steady velocity field and uniform distribution of the dispersed particle phase and gas phase properties over the cross section of the channel. By summing all the contributions arising from the entire kth class, we obtain the system of equations

$$\begin{aligned}
&n_{p_k} = \frac{n_{pk0} u_{pk0}}{u_{pk}}, \\
&\frac{\mathrm{d}}{\mathrm{d}\,x}(u_{p_k}) = \frac{1}{u_{p_k}} \frac{u_g - u_{p_k}}{\tau_{p_k}}, \\
&\frac{\mathrm{d}}{\mathrm{d}\,x}(T_{p_k}) = \frac{\epsilon_p I_0 A_{p_k}}{m_{p_k} u_{p_k} C_{vp}} + \frac{\pi D_{p_k}^2 h_{p_k}}{m_{p_k} u_{p_k} C_{vp}} \left(T_g - T_{p_k}\right), \\
&\frac{\mathrm{d}}{\mathrm{d}\,x}(T_g) = \frac{\pi}{\rho_0 u_0 C_P} \sum_{k=1}^{N_S} n_{p_k} D_{p_k}^2 h_{p_k} (T_{p_k} - T_g), \\
&u_g = \frac{T_g}{T_0} u_0.
\end{aligned} \tag{3.1}$$

The solution of this system is obtained using a first-order forward discretization of the spatial derivative and the explicit evaluation of the temperature difference between flow and particle.

To compare the results of DNS to the predictions of the 1D model, we employ an averaging in the spanwise and vertical directions and a time span 2τ in the steady state, so that for any quantity, $q(x, y, z, t)$ simulated in DNS,

$$\overline{q}(x) = \frac{1}{2\tau W^2} \int_{t-\tau}^{t+\tau} \left(\int_{\partial \mathcal{V}_x} q(x, y, z, t^{'}) \mathrm{d}y \mathrm{d}z \right) \mathrm{d}t', \tag{3.2}$$

where $\mathcal{V}_{\S}$ is the cross section of the channel at location x. Another interesting diagnostic is the volume and time averaged quantity, defined as

$$\langle q \rangle = \frac{1}{2\tau \mathcal{V}} \int_{t-\tau}^{t+\tau} \left(\int q(x, y, z, t^{'}) \right) \mathrm{d}t'. \tag{3.3}$$

Figure 1 shows the comparison between the averaged gas and particle temperatures and velocities from DNS and 1D model for polydisperse and monodisperse simulations at $St_{\eta_0} = 1.0$. These are the cases for which the preferential concentration of particles is the most pronounced. The DNS average particle temperatures are higher than the predictions of the 1D model throughout the channel. This is because of higher residence times of particles in the channel in DNS compared to the 1D model. This difference is seen in the particle number density, presented in Figure 2, which shows that although n in DNS follows the same decreasing trend in 1D model due to particle dilution, the number density of particles from DNS is generally higher. This difference accounts for more radiation absorption, and higher temperature of particles. The difference between the DNS and the 1D model for gas temperature in Figure 1 is, however, much less, since the heat transfer to the gas becomes at the same time less efficient when particles accumulate in the channel and cluster more. Figure 1 also shows that polydisperse particles are heated considerably less than monodisperse particles while the gas temperature does not exhibit a large difference by using either of the particles. Less heating of polydisperse particles is because the relative rate of radiation absorption to the rate of conductive heat transfer from the particles is smaller for polydisperse particles, i.e., compare $\mathcal{R}^{\mathrm{SA}}$ to $\mathcal{R}^{\mathrm{mono}}$ in Table 1. Meanwhile, polydisperse particles exhibit a higher efficiency in heat transfer to the gas. Less clustering of particles for polydisperse particles, as seen in Figure 2 and to be seen later in Section 5, also contributes to this higher heat transfer efficiency.

4. Energy balance

The total energy E^t of the mixture can be expressed as the contribution of the two phases E_g^t and E_p^t, each consisting of their internal, potential and kinetic parts, where

$$\begin{aligned} E^t &= E_g^t + E_p^t, \\ E_g^t &= \rho e_g + \frac{1}{2}\rho|\vec{\boldsymbol{u}}^2| + \rho|\vec{\boldsymbol{g}}|z \simeq \rho e_g = \rho C_v T_g, \\ E_p^t &= \sum_{k=1}^{N_s} \sum_{j=1}^{N_{p_k}} m_{p_k} \left(C_{vp} T_{p,j} + \frac{1}{2}|\vec{\boldsymbol{u}}_{p,j}^2| + \rho_p |\vec{\boldsymbol{g}}| z_{p,j} \right) \simeq \sum_{k=1}^{N_s} \sum_{j=1}^{N_{p_k}} m_{p_k} C_{vp} T_{p,j}. \end{aligned} \tag{4.1}$$

In the equations above we have made use of our zero gravity assumption, and neglected the kinetic energy parts as they are at least 4 orders of magnitude smaller than the

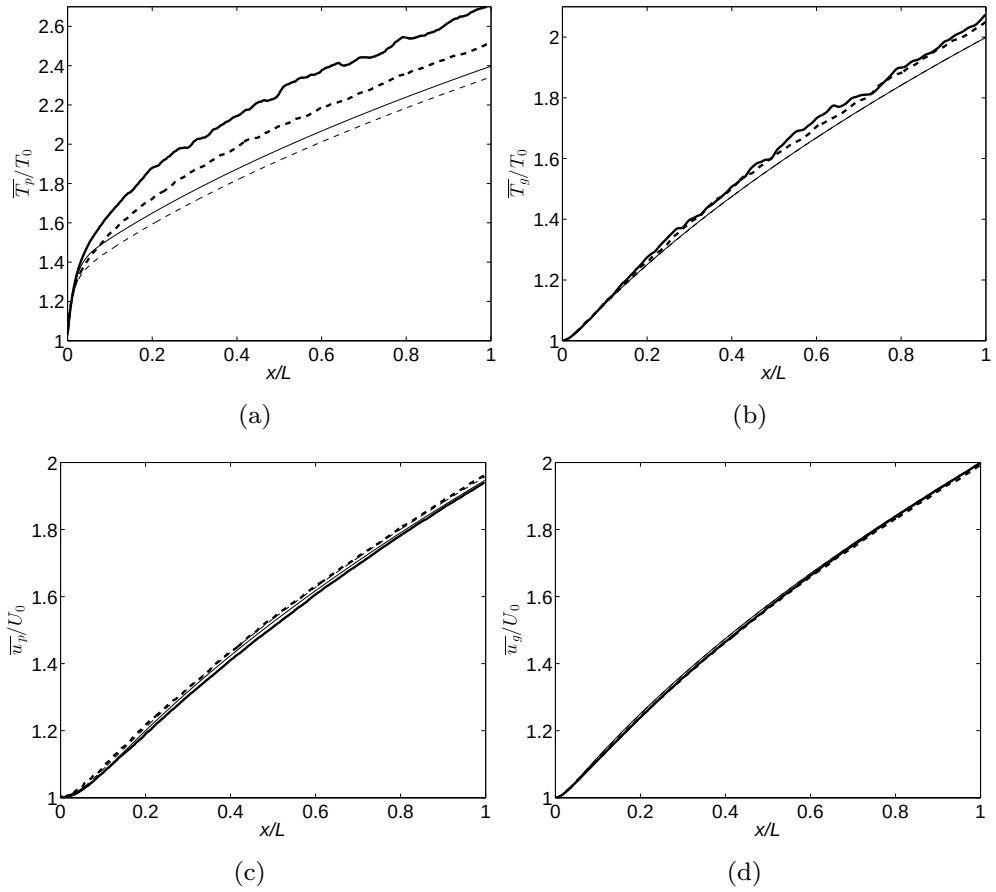

Figure 1: Variations of the averaged particle temperature (a), gas temperature (b), particle velocity (c), and gas velocity (d), along the streamwise direction of the channel for the $St_{\eta_0} = 1.0$ case. In each panel the thick lines indicate DNS and the thin lines 1D model, the solid lines delineate monodisperse particle simulation, and the dashed lines the equivalent polydisperse particles simulation.

thermal energy parts. The internal energy of gas balance is stated by the following conservation equation

$$\frac{\partial(\rho e_g)}{\partial t} + \boldsymbol{\nabla}\cdot(\rho e_g \vec{\boldsymbol{u}}) + P\,\boldsymbol{\nabla}\cdot\,\vec{\boldsymbol{u}} = \Phi + k\boldsymbol{\nabla}^{\mathbf{2}}T_g + \mathcal{S}, \tag{4.2}$$

where Φ is used to collect all the terms related to viscous stress dissipation (which is negligible), and $k\boldsymbol{\nabla}^{\mathbf{2}}T_g$ represents the thermal energy fluxes due to the conduction effects. By making use of the enthalpy definition for a polytropic ideal gas, $h = C_P T_g$, and neglecting the contributions related to dissipation and conduction the final form reads

$$\frac{\partial(\rho e_g)}{\partial t} + \boldsymbol{\nabla}\cdot(\rho h \vec{\boldsymbol{u}}) = \mathcal{S}. \tag{4.3}$$

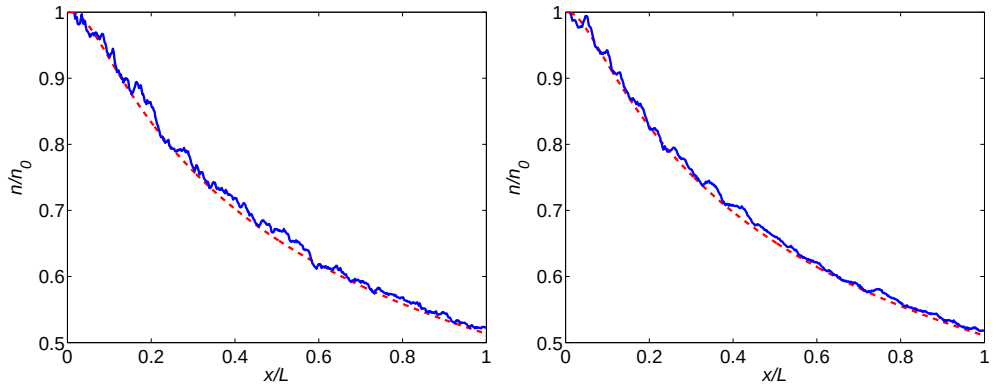

Figure 2: Variations of the averaged particle number density normalized by its inlet value for monodisperse particles (a), and polydisperse particles (b) for $St_{\eta_0} = 1.0$ (case 3 in Table 1). The solid lines delineate the monodisperse particle simulation, and the dashed lines the equivalent polydisperse particles simulation in both panels.

By integrating the equation above over the entire volume of the channel, the total energy balance for the gas phase is obtained as

$$\int_{\partial\mathcal{V}_{\text{out}}} \rho h \vec{\boldsymbol{u}} \cdot \vec{\boldsymbol{n}} \, \mathrm{d}\partial\mathcal{V}_{\text{out}} + \int_{\partial\mathcal{V}_{\text{in}}} \rho h \vec{\boldsymbol{u}} \cdot \vec{\boldsymbol{n}} \, \mathrm{d}\partial\mathcal{V}_{\text{in}} = \int_{\mathcal{V}} \mathcal{S} \, \mathrm{d}\mathcal{V}, \tag{4.4}$$

which states that the difference in the flux of enthalpy at the outlet and inlet is equal to the rate of heat transfer from the particles to the gas in the channel.

The equation of the internal energy for a single particle in a Lagrangian form is

$$\frac{d}{dt}\left(m_p C_{vp} T_p\right) = \epsilon_p A_p I_0 + \pi h_p D_p^2 \left(T_g(\vec{\boldsymbol{x}}_p) - T_p\right). \tag{4.5}$$

Converting this equation to Eulerian frame (the details given in Rahmani *et al.* 2015), and averaging over the volume of the channel yields

$$\frac{1}{L} C_{vp} \sum_{k=1}^{N_S} m_{p_k} \sum_{j=1}^{N_{p_k}} \left(u_{p,j} T_{p,j}\big|_{\text{out}} - u_{p,j} T_{p,j}\big|_{\text{in}} \right) = \epsilon_p I_0 \sum_{k=1}^{N_S} N_{p_k} A_{p_k} - \int_{\mathcal{V}} \mathcal{S} \, \mathrm{d}\mathcal{V}, \tag{4.6}$$

which describes the energy balance for particles in the system; the increase in the thermal energy of the particles at the outlet is equal to the rate of radiation absorption by particles minus the rate of heat transfer from particles to the gas. A total energy balance for the system can be obtained by summing Eqs. (4.4) and (4.6):

$$\rho h u\big|_{\text{out}} - \rho h u\big|_{\text{in}} + \frac{1}{\mathcal{V}} C_{vp} \sum_{k=1}^{N_S} m_{p_k} \sum_{j=1}^{N_{p_k}} \left(u_{p,j} T_{p,j}\big|_{\text{out}} - u_{p,j} T_{p,j}\big|_{\text{in}} \right) = \frac{\epsilon_p I_0}{W^2} \sum_{k=1}^{N_S} N_{p_k} A_{p_k}. \tag{4.7}$$

This equation states that the sum of the gains in the flux of the thermal energy for gas and particle phases should balance the input radiation in the channel. Equation 4.7 can be non-dimensionalized by $n_p \rho_p C_{vp} T_0 U_0 / L$, the convective transfer rate of thermal

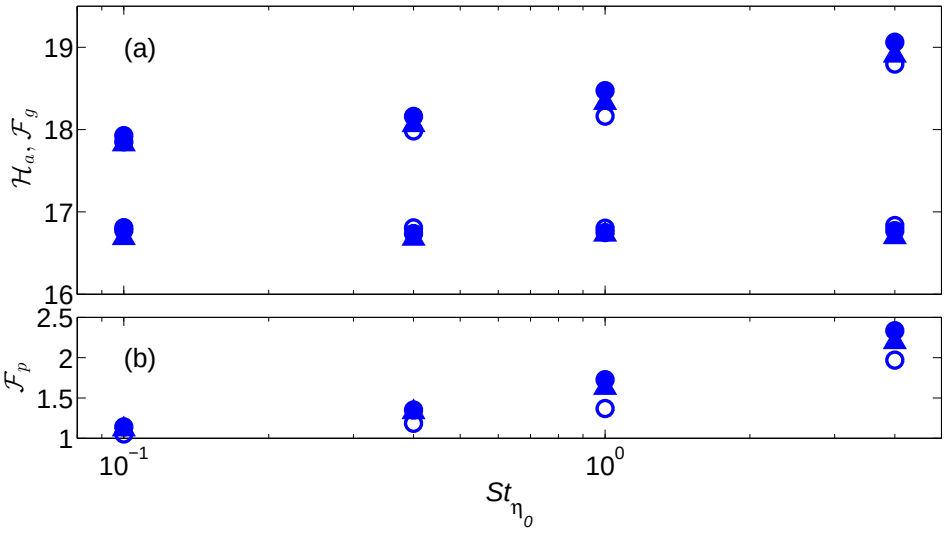

Figure 3: Time-averaged nondimensional rates of the total radiation absorption, $\mathcal{H}_a$ (panel (a), higher values), gas internal energy flux increase at the outlet, $\mathcal{F}_g$(panel (a), lower values), and particle internal energy flux increase at the outlet , $\mathcal{F}_p$ (bottom panel), for different cases. Filled circles indicate DNS monodisperse particles, empty circles show 1D monodisperse particles, and filled triangles show polydisperse particles.

energy of a particle, so that Eq. 4.7 reads

$$\mathcal{F}_g + \mathcal{F}_p = \mathcal{H}_a, \tag{4.8}$$

where $\mathcal{F}_g$ and $\mathcal{F}_p$ are the dimensionless increase in the flux of thermal energy of gas and particles, and $\mathcal{H}_a$ is the dimensionless rate of radiation absorption by the particles, and these quantities are averaged over the time span 2τ in the steady state.

Figure 3 shows these dimensionless rates for different simulations. Out of the input energy, more than 85% is harvested through $\mathcal{F}_g$, while the remaining portion is obtained from $\mathcal{F}_p$. Higher Stokes number cases absorb more radiation over the entire volume of the channel as particles have higher residence times for these cases. But this higher input energy is only carried by the particles since the gas thermal relaxation time, $\tau_{gth} = \rho_0 C_p/(2\pi k n_0 D_p)$, also increases with increasing Stokes number. Compared to monodisperse particles, polydisperse particles gain lower values of $\mathcal{H}_a$ values, suggesting that the averaged particle concentration in the channel is lower for polydisperse particles. This lower radiation absorption results in both lower $\mathcal{F}_g$ and $\mathcal{F}_p$ for polydisperse particles. Similar to its predictions for the outlet temperature, the one-dimensional model underestimates the radiative heat absorption by particles and the thermal energy flux increase of the particle phase, as this model neglects the more complex particle concentration patterns that can occur in DNS.

5. Preferential concentration

To quantify particle-clustering patterns, we employ radial distribution functions (RDF). For different streamwise locations along the channel, we find all particles that are located within a small distance from that streamwise location and assume that all these particles

are located on the same two-dimensional plane. An RDF for these particles is defined as (Ray & Collins 2011)

$$g(r) = \frac{N_r A}{N A_r}, \tag{5.1}$$

where N_r is the number of particle pairs in a disc element with area A_r and radius r from a sample particle location, N is the total number of particle pairs on the plane, and A is the cross-sectional area of the plane, i.e., W^2.

Figure 4 shows the instantaneous snapshots of particle distribution for case 3 of Table 1, together with the time-averaged RDFs at different locations along the channel. At $St_{\eta_0} = 1.0$, monodisperse particles are strongly preferentially concentrated, as expected from the knowledge established in previous studies, with g reaching values up to 7 times higher than the uniform particle distribution. This causes highly nonuniform particle concentrations and temperatures along the channel and at the outlet. Preferential concentration generates areas of highly concentrated and hot particles, besides large patches of void areas. As turbulence decays along the channel, however, values of the function g decrease. Polydisperse particles, when examined as a whole, exhibit less preferentially concentrated particles, as also indicated by significantly lower values of g. One reason is that $St_{\eta_0}^{\mathrm{SA}} = 0.8$ for this case, which brings the effective overall Stokes number lower than 1.0. Moreover, we speculate that different behavior of different classes of particles and potential segregation of particles based on their size prevents particles from showing a distinctive particle-clustering pattern.

To examine this conjecture, we test the behavior of particles per class, also presented in Figure 4. The clustering snapshots and the RDF analysis are shown for 3 different classes of particle size, after dividing the entire PDF of particle size to 5 equal sections, i.e., $N_S = 5$. The first class shown in Figure 4 represents the smallest particles with a sample-averaged Stokes number of 0.32 for the class, the second class shown is the mid-size particles with the class sample-averaged Stokes number of 0.91, and the last class shows the largest particles with per class sample averaged Stokes number of 1.82. The snapshots of the particle distribution show that the clustering patterns are clearly different for each class of particle size. Larger particles form clusters and voids at significantly larger scales as they interact with larger-size eddies in the flow. This causes segregation of particle classes. The RDF analysis shows that the preferential concentration is the highest for the class with sample-averaged Stokes number closest to one, i.e., the second class shown. A feature specific to polydisperse particles is that they exhibit significantly more preferential concentrations closer to the inlet. This is clearly a characteristic of larger particles in particular, which we ascribe to the hydrodynamic and thermodynamic interactions with other classes of particles through the gas phase that contribute to the more uniform distribution of large particles.

The discussion above suggests that each particle class in a polydisperse set of particles may behave differently from its Stokes number equivalent monodisperse particle. Figure 5 shows the maximum value of function g collected from an RDF analysis at different locations in the channel for monodisperse particles as a function of their local Stokes number, for polydisperse particles as a function of their sample-averaged local Stokes number, and for different classes of particles as a function of their local sample-averaged Stokes number per that class (when dividing the PDF to 5 sections). This figure indicates that the trend of change of $g^{\max}$ with St_η for monodisperse particles, that peaks at $St_\eta \sim 1$, is in agreement with previous studies. The sample averaging of the Stokes number over the entire classes of particles for polydisperse particles, however, does not

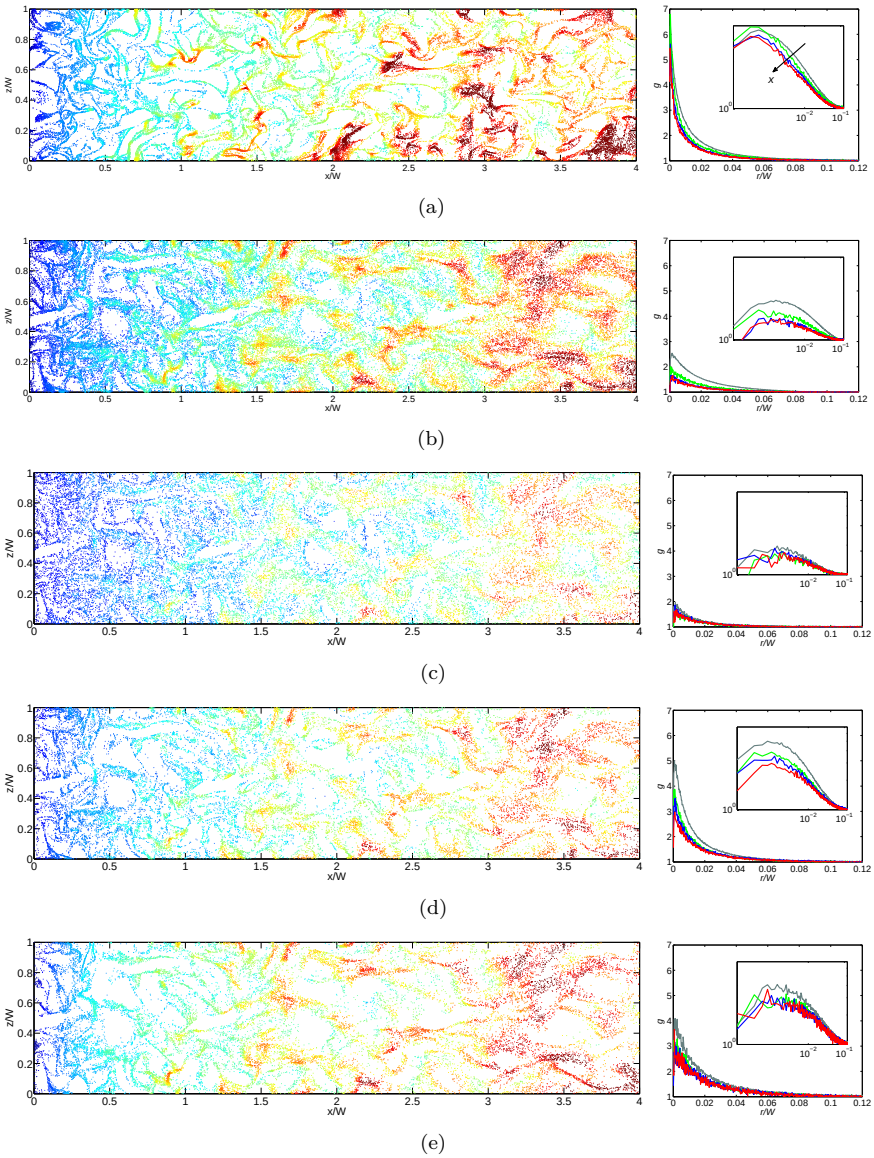

(a)

(b)

(c)

(d)

(e)

Figure 4: Snapshots of the instantaneous particle concentrations for case 3 of Table 1: (a) monodisperse particles, (b) polydisperse particles, (c) polydisperse, class 1 particle size (d) polydisperse, class 3 particle size , and (e) polydisperse, class 5 for an $N_S = 5$ section division. The panels on the right show the RDF computation for each particle case at $x/L_x = 1/10$, $1/2$, $3/4$ and 1.0. The RDF curves drop when propagating along the streamwise direction in the channel. The insets show the same plots on a log-log scale.

seem to be a good measure for representations of particle clustering. When RDF analysis is performed for each class, and $g^{\max}$ plotted versus the sample-averaged Stokes number per that class, the pattern is closer to that of monodisperse particles. However, still

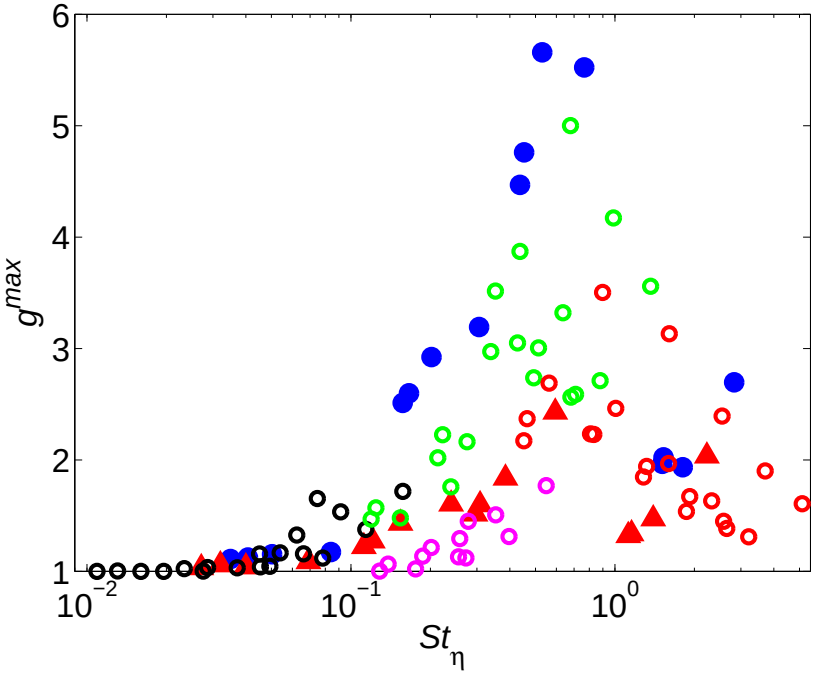

Figure 5: Variation of $g^{\max}$ with St_η for monodisperse particle (filled circles), polydisperse particles, the entire PDF (filled triangles), and different classes (5 total classes) of polydisperse particles (empty circle). The data are obtained from all simulations in Table 1 sampled at different locations along the channel at $x/L_x = 1/10$, $1/2$, $3/4$, and 1.0.

the behavior is distinct from monodisperse particles at the same Stokes number. This difference suggests that the interactions between classes may inhibit or enhance particle clustering of individual particle size classes.

6. Conclusions

In this study, we have performed DNS of flows laden with polydisperse particles and compared them to flows laden with thermodynamically equivalent monodisperse particles, where the mass loading ratio and the total frontal area of particles have been matched between the two systems. We compare the DNS results to the predictions of a 1D model that assumes uniform gas properties and particle distribution over the cross section of the channel. Due to nonuniformities in particle distribution at higher Stokes numbers and higher particle residence times, the averaged DNS particle temperatures are up to 10% higher than the predictions of the 1D model. The DNS averaged gas temperature, and both phases velocities are, however, in a good agreement with the 1D model.

Our investigation of the energy balance for the entire system shows that for our design of particles, the gas phase is the main carrier of the energy. Slower particle motion and more nonuniformities in particle concentration at higher Stokes numbers enhance the radiation absorption and particle thermal energy fluxes. However, this is at the cost of less efficient heat transfer to the gas and therefore does note translate into more heating

of the gas. So, for all our simulations, regardless of their clustering pattern, the gain in the flux of gas energy compared to the input flux of particle energy remained fairly constant. The 1D model could predict this gain in gas energy flux within 10% discrepancy.

Our classification of monodisperse particle concentration based on the Stokes number was in agreement with widely available previous studies, with the consensus that the particles are strongly preferentially concentrated close to the Stokes number of unity. For polydisperse particles, however, we have shown that the sample-averaged Stokes number over all classes is not a reliable indicator of the particle concentration pattern. In particular, wherever different classes in polydisperse particles represent a wide range of Stokes numbers above and below one, identifying a dominant concentration pattern was not feasible. All our polydisperse particles exhibited less particle clustering, as measured by RDF, compared to their monodisperse equivalent particles. By examining classes of particles individually, we obtained a more distinctive particle clustering pattern per class. However, these individual classes were still less preferentially concentrated compared to monodisperse particle with similar Stokes numbers in most cases. The more uniformly distributed polydisperse particles were more efficient in transferring the heat to the gas and, hence, generated a more uniform gas temperature field.

For future work, examining the effects of turbulence intensity, walls and shear on the thermal performance of particle solar receivers, laden with polydisperse particles, will be interesting topics to explore.

Acknowledgments

This investigation was funded by the Advanced Simulation and Computing (ASC) program of the US Department of Energy's National Nuclear Security Administration via the PSAAP-II Center at Stanford. We are thankful to Mahdi Esmaily-Moghadam and Jeremy Horowitz for their invaluable comments for improving this report.

REFERENCES

Balachandar, S. & Eaton, J. K. 2010 Turbulent dispersed multiphase flow. *Annu. Rev. Fluid Mech.* **42**, 111–133.

Eaton, J. K. & Fessler, J. 1994 Preferential concentration of particles by turbulence. *Int. J. Multiphase Flow* **20**, 169–209.

Elghobashi, S. & Truesdell, G. 1993 On the two-way interaction between homogeneous turbulence and dispersed solid particles. I: Turbulence modification. *Phys. Fluids* **5** (7), 1790–1801.

Eswaran, V. & Pope, S. 1988 An examination of forcing in direct numerical simulations of turbulence. *Comput. Fluids* **16** (3), 257–278.

Maxey, M. 1987 The gravitational settling of aerosol particles in homogeneous turbulence and random flow fields. *J. Fluid Mech.* **174**, 441–465.

Pouransari, H. & Mani, A. 2015 On the effects of preferential concentration on heat transfer in particle-based solar receivers. Submitted to *J. Fluid Mech.*

Rahmani, M., Geraci, G., Iaccarino, G. & Mani, A. 2015 On polydispersity of particles in an irradiated turbulent gas-particle mixture. Submitted to *J. Fluid Mech.*

Ray, B. & Collins, L. R. 2011 Preferential concentration and relative velocity statistics of inertial particles in Navier–Stokes turbulence with and without filtering. *J. Fluid Mech.* **680**, 488–510.

Rosales, C. & Meneveau, C. 2005 Linear forcing in numerical simulations of isotropic turbulence: Physical space implementations and convergence properties. *Phys. Fluids* **17** (9), 095106.

Siegel, N. P., Ho, C. K., Khalsa, S. S. & Kolb, G. J. 2010 Development and evaluation of a prototype solid particle receiver: on-sun testing and model validation. *J. Sol. Energy Eng.* **132** (2), 021008.

Squires, K. D. & Eaton, J. K. 1991 Preferential concentration of particles by turbulence. *Phys. Fluids* **3** (5), 1169–1178.

Sundaram, S. & Collins, L. R. 1999 A numerical study of the modulation of isotropic turbulence by suspended particles. *J. Fluid Mech.* **379**, 105–143.

Zamansky, R., Coletti, F., Massot, M. & Mani, A. 2014 Radiation induces turbulence in particle-laden fluids. *Phys. Fluids* **26** (7), 071701.